Progress In Electromagnetics Research M, Vol. 47, 13–25, 2016

Study on Radial Suspension Force of Single Winding Bearingless Induction Motor Based on Two-Fundamental Wave Method

Ze Bin Yang*, Ren Jin, Xiao Dong Sun, and Wei Yu Zhang

Abstract—The radial suspension force with a new structure of a bearingless induction motor based on single winding is researched. Compared to the conventional double-winding structure of bearingless induction motor, torque and suspension forces are produced with a single-winding system. Bearingless induction motor is a nonlinear, multi-variable and strong coupling system. It is difficult to obtain an accurate mathematical model on the radial suspension force. So the research method about radial suspension force of a single-winding bearingless induction motor is proposed, based on two fundamentals. Firstly, a new structure and operation principle of a single-winding bearingless induction motor is introduced. Then the air gap flux density distribution of the single-winding bearingless induction motor is analyzed in detail. The accurate mathematical model of radial suspension force is deduced by using two-fundamental wave method and Maxwell's stress tensor method. Secondly, according to the transient analysis of the single-winding bearingless induction motor in which its speed is 6000 r/min by finite element method (FEM), the component of radial suspension force in x-axis and y-axis is obtained by FEM simulation analysis. The calculation results used by FEM and the theoretical calculation results of mathematical model used by two-fundamental wave method have been compared. Thirdly, an experimental prototype is produced, and suspension experiment of prototype is carried out. Then measured result of radial suspension force is analyzed. The analysis results show that the prototype has excellent suspension characteristics, and the mathematical model of radial suspension force based on two-fundamental wave method has low error and high precision.

1. INTRODUCTION

The advantages of traditional asynchronous motor such as simple structure, low cost, high reliability, uniform air gap, easy weak magnetic control and small cogging torque are contained in bearingless induction motor (BIM). The advantages of no friction, no wear, no lubrication and sealing, high speed, high precision, long life are also included in a bearingless induction motor. In special circumstances, such as high speed and ultrahigh speed, vacuum, clean, and corrosion, the motor can achieve a stable supporting operation under the condition of "no bearing". In aerospace, flywheel energy storage, high speed gyro, magnetic suspending hard disk drive, artificial heart pump, energy chemical industry and other special electric drive/transmission fields, BIM has broad application prospects [1–3].

At present, a double-winding structure is accepted in BIM to realize the suspension and rotation of a rotor [4]. A set of radial suspension force winding used for supporting the rotor suspended is overlapped on the stator winding used for driving motor rotated. So the practical application of a bearingless induction motor is restricted, for reasons of the complexity of the motor design and manufacture process increased by double-winding structure, high winding insulation requirements, low copper factor, high flux leakage of motor, reduced reliability of a motor.

Received 19 January 2016, Accepted 8 March 2016, Scheduled 17 March 2016

* Corresponding author: Ze Bin Yang (zbyang@ujs.edu.cn).

The authors are with the College of Electrical & Information Engineering, Jiangsu University, No. 301 Xuefu Road, Zhenjiang, Jiangsu Province 212013, P. R. China.

Aimed at the shortcoming of a double-winding structure, a new structure of BIM based on single winding is put forward. The suspension and rotation of the rotor is implemented by this new structure with only a single winding. At the same time, the cost of a single-winding bearingless induction motor is greatly reduced, being conducive to the industrialization of magnetic suspension motor. And the copper factor of a motor is guaranteed, because of no necessity to add the insulation materials between double-winding for reducing the flux leakage of motor. Meanwhile, the structural redundancy of a single-winding motor and fault-tolerant control for windings are easily implemented. Then the motor can realize more reliable operation.

The internal magnetic field of a single-winding bearingless induction motor is analyzed, using Ansoft/Maxwell finite element analysis software. An accurate mathematical model of radial suspension force for the single-winding bearingless induction motor is deduced based on the principle of radial suspension force in traditional BIM. The radial suspension force is calculated based on two-fundamental wave method. The simulation results are compared with those obtained from experimental measurements with Matlab software. The finite element analysis of radial suspension forces is in good agreement with that of the mathematical models, thereby the accuracy and effectiveness of the theory are verified.

2. THE STRUCTURE AND THE BASIC WORKING PRINCIPLE OF PRODUCING RADIAL SUSPENSION FORCES OF A SINGLE-WINDING BEARINGLESS INDUCTION MOTOR

Two different kinds of electromagnetic forces, Lorentz force and Maxwell force exist in conventional rotatory motor. Lorentz force is generated by the rotating magnetic field interacting with current-carrying conductor, also known as Ampere force. It is acted on the surface of the rotor along the circle tangent, mainly producing electromagnetic torque which makes the motor rotate. Maxwell force is magnetic tension force generated on the border from various permeabilities of ferromagnetic material (core and air). It is perpendicular to the surface of the rotor, mainly showing as radial magnetic tension force. However, aiming at BIM, the role of Lorentz force in suspension control is relatively small and negligible. So the Maxwell force is mainly researched. In a double-winding structure of stator slot in BIM, torque winding (p_1-pair pole, ω_1 electrical angular frequency) and radial suspension force winding (p_2-pair pole, ω_2 electrical angular frequency) are compound intertwined. The controllable suspension force is generated in the motor, satisfied by $p_1 = p_2 \pm 1$ and $\omega_1 = \omega_2$ [5, 6].

In a traditional double-winding structure of BIM, torque magnetic field and suspension magnetic field are generated respectively by two windings. However, in a single-winding bearingless induction motor, torque magnetic field and suspension magnetic field are generated by only one winding. For the rotor, two different kinds of structures above are equivalent. In the structure of a single-winding bearingless induction motor, stator current is regarded as the combination of two current components. The torque magnetic field and suspension magnetic field are generated respectively by two current components. The two current components are regarded respectively as torque current component and suspension current component.

Figure 1 shows that $i_1 \sim i_6$ are defined as stator winding currents. So i_k can be expressed as:

$$\begin{aligned} i_k &= i_{tk} + i_{sk} \\ k &= 1 \ldots 6 \end{aligned} \tag{1}$$

where i_k is the stator winding current, i_{tk} the stator torque current component, and i_{sk} the stator suspension current component [7–9].

Figure 2 shows that two-pole torque magnetic field is generated when torque current component is only imported in the single-winding bearingless induction motor. Fig. 3 shows that four-pole suspension magnetic field is generated when suspension current component is only imported in a single-winding bearingless induction motor. The superposition magnetic field is produced, which consists of two-pole magnetic field and four-pole magnetic field when the torque current component and suspension current component are simultaneously imported in the single-winding bearingless induction motor. The air gap flux density on positive direction in y-axis is enhanced, and the air gap flux density on negative direction in y-axis is reduced by superposition magnetic field. The radial suspension force defined as F_y is

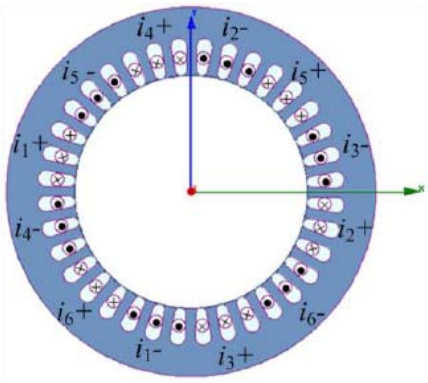

Figure 1. Distribution of the stator winding current.

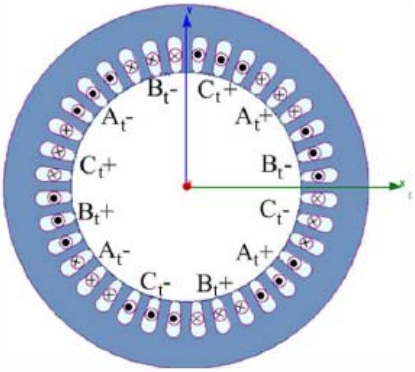

Figure 2. Distribution of torque component on stator winding.

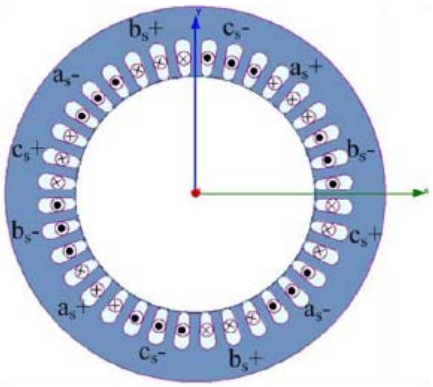

Figure 3. Distribution of suspension component on stator winding.

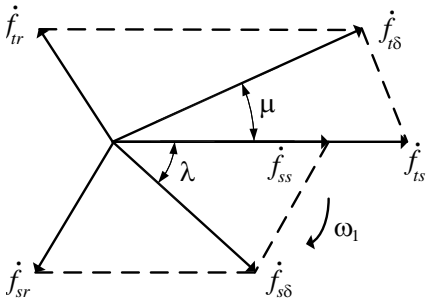

Figure 4. Schematic diagram of magnetomotive force.

generated on positive direction in y-axis by unbalanced air gap flux. At the same time, radial suspension force along negative direction in y-axis is generated on the rotor, when torque current component and suspension current component at negative direction are simultaneously imported in the single-winding bearingless induction motor. In the same way, the radial suspension force in x-axis is obtained [10, 11].

3. THE MATHEMATICAL MODEL OF RADIAL SUSPENSION FORCE ON THE SINGLE-WINDING BEARINGLESS INDUCTION MOTOR

The magnetic potential vector graph about the single-winding bearingless induction motor is shown in Fig. 4, where f_{ts} and f_{ss} are stator magnetomotive forces which are respectively produced by torque current component and suspension current component; f_{tr} and f_{sr} are rotor magnetomotive forces which are respectively produced by torque current component and suspension current component; $f_{t\delta}$ and $f_{s\delta}$ are air gap magnetomotive forces which are respectively produced by torque current component and suspension current component.

So the Maxwell force acting on the surface of the rotor can be expressed as:

$$df = \frac{\mu_{\mathrm{Fe}} - \mu_0}{2\mu_{\mathrm{Fe}}\mu_0}\left(B^2 + \mu_{\mathrm{Fe}}\mu_0 H\right) dA \approx \frac{B^2 dA}{2\mu_0} \tag{2}$$

where μ_{Fe} and μ_0 are respectively the core permeability and air gap permeability; μ_0 is far lower than μ_{Fe}; dA is the unit area of rotor's surface; B is the magnetic induction along the normal direction on interface between corn and air gap; H is the magnetic induction along the tangential direction on

interface between corn and air gap. Because magnetic lines of force is almost vertically in and out of the core, $H \approx 0$ is feasible [12].

When $A = lr\gamma$ is substituted into Eq. (2), the Maxwell force can be expressed as:

$$df = \frac{lrB^2 d\gamma}{2\mu_0} \tag{3}$$

where l is the core length, r the external radius of rotor, and γ the angle between arbitrary position and x-axis.

1) Neglected magnetic saturation, eddy current Loss and stator magnetic potential harmonic, no rotor eccentricity are assumed. The total synthetic air gap flux density in the single-winding bearingless induction motor can be expressed as:

$$B_x(\gamma, t) = B_{TX}\cos(\omega_1 t - p_1\gamma - \mu) + B_{SX}\cos(\omega_2 t - p_2\gamma - \lambda) \tag{4}$$

where B_{TX} is the amplitude of air gap flux density formed by torque current component, B_{SX} the amplitude of air gap flux density formed by suspension current component, λ the preliminary angle on air gap flux linkage produced by suspension current component in dq coordinate, and μ the preliminary angle on air gap flux linkage produced by torque current component in dq coordinate.

As shown in Equation (3), the Maxwell force acting on unit area of rotor's surface can be expressed as:

$$df(\gamma, t) = \frac{lr}{2\mu_0}\left[B_{TX}\cos(\omega_1 t - p_1\gamma - \mu) + B_{SX}\cos(\omega_2 t - p_2\gamma - \lambda)\right]^{2d}\gamma \tag{5}$$

Integrating Equation (5) along circle air gap of motor, the component of Maxwell force in x-axis can be expressed as:

$$\begin{aligned} f_x &= \int_0^{2\pi} \frac{lr}{2\mu_0}\left[B_{TX}\cos(\omega_1 t - p_1\gamma - \mu) + B_{SX}\cos(\omega_2 t - p_2\gamma - \lambda)\right]^2 \cos\gamma \mathrm{d}\gamma \\ &= \frac{lr}{4\mu_0} B_{TX}B_{SX}\int_0^{2\pi}\Big\{\cos\left[(p_1 - p_2 - 1)\gamma + (\omega_2 - \omega_1)t - (\mu - \lambda)\right] \\ &\quad + \cos\left[(p_1 - p_2 + 1)\gamma + (\omega_2 - \omega_1)t - (\mu - \lambda)\right]\Big\}\mathrm{d}\gamma \end{aligned} \tag{6}$$

When $p_1 - p_2 \pm 1 = 0$ and $\omega_1 = \omega_2$ are both established, f_x is a controllable variable. Supposing that $p_1 = 1$ and $p_2 = 2$, the Maxwell force can be expressed as:

$$\begin{aligned} f_x &= \frac{lr}{4\mu_0} B_{TX}B_{SX}\int_0^{2\pi}\cos(-2\gamma + \lambda - \mu)\mathrm{d}\gamma + \frac{lr}{4\mu_0} B_{TX}B_{SX}\int_0^{2\pi}\cos(\lambda - \mu)\mathrm{d}\gamma \\ &= 0 + \frac{lr}{4\mu_0} B_{TX}B_{SX}2\pi\cos(\lambda - \mu) = \frac{\pi lr}{2\mu_0} B_{TX}B_{SX}\cos(\lambda - \mu) \end{aligned} \tag{7}$$

In the same way, the component of Maxwell force in y-axis can be expressed as:

$$f_y = \frac{\pi lr}{2\mu_0} B_{TX}B_{SX}\sin(\lambda - \mu) \tag{8}$$

2) When rotor eccentricity occurs, the flux density of air gap is no longer in equality. δ can be calculated by the following method.

Figure 5 shows that δ_0 can be defined as the average air gap length when the rotor has no eccentricity. e can be defined as eccentricity of the rotor when circle center of the stator is the origin. γ_s can be defined as the angle between eccentric direction of the rotor and x-axis direction. γ can be defined as the angle between arbitrary location in air gap and x-axis direction.

Defined as $\tau = e/\delta_0$, air gap length in arbitrary direction can be expressed as $\delta(\gamma) = \delta_0[1 - \tau\cos(\gamma - \gamma_s)]$.

Eccentricities of the stator and rotor respectively resolve along x-axis direction and y-axis direction.

$$\begin{cases} x = e\cos\gamma_s \\ y = e\sin\gamma_s \end{cases} \tag{9}$$

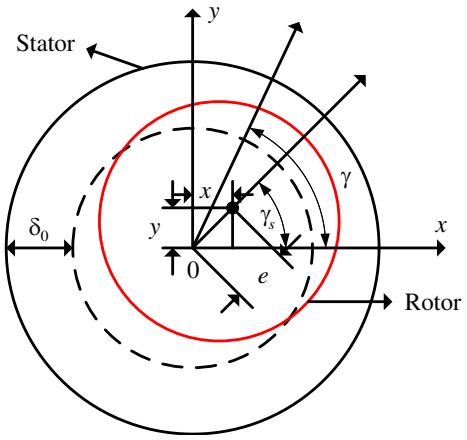

Figure 5. Distribution of air gap considering the rotor eccentricity.

where $e = \sqrt{x^2 + y^2}$ is defined.

So air gap length in arbitrary direction can be expressed as:

$$\delta(\gamma) = \delta_0 - e\cos(\gamma - \gamma_s) = \delta_0 - x\cos\gamma - y\sin\gamma \tag{10}$$

In the same way,

$$\frac{1}{\delta} = \frac{1}{\delta_0 - x\cos\gamma - y\sin\gamma} \approx \frac{1}{\delta_0}\left(1 + \frac{x}{\delta_0}\cos\gamma + \frac{y}{\delta_0}\sin\gamma\right) \tag{11}$$

$$\begin{cases} B_{TX}(\delta) = B_{TX}\left(1 + \dfrac{x}{\delta_0}\cos\gamma + \dfrac{y}{\delta_0}\sin\gamma\right) \\ B_{SX}(\delta) = B_{SX}\left(1 + \frac{x}{\delta_0}\cos\gamma + \dfrac{y}{\delta_0}\sin\gamma\right) \end{cases} \tag{12}$$

On the basis of Maxwell's stress tensor method, the radial suspension force is subjected on the area which is defined as $d\gamma$ of the rotor's surface along electrical angle γ. The force decomposed along x-axis can be expressed as [13]:

$$\begin{aligned} f_x &= \int_0^{2\pi} \frac{lr}{2\mu_0}\left[B_{TX}(\delta)\cos(\omega_1 t - p_1\gamma - \mu) + B_{SX}(\delta)\cos(\omega_2 t - p_2\gamma - \lambda)\right]^2\cos\gamma \mathrm{d}\gamma \\ &= \frac{\pi lr B_{TX}B_{SX}}{2\mu_0}\cos(\mu - \lambda) + \frac{\pi lr B_{TX}B_{SX}\tau^2}{4\mu_0}\cos(\mu - \lambda) + \frac{\pi lr B_{TX}B_{SX}\tau^2}{8\mu_0}\cos(\mu - \lambda \pm 2\gamma_s) \\ &\quad + \frac{\pi lr B_{TX}B_{SX}\tau^2}{8\mu_0}\cos(2\omega t - \mu - \lambda - 2\gamma_s) + \frac{\pi lr\tau\left(B_{TX}^2 + B_{SX}^2\right)}{2\mu_0}\cos\gamma_s \\ &\quad + \frac{\pi lr B_{TX}^2\tau}{4\mu_0}\cos(2\omega t - 2\mu - \gamma_s) + \frac{\pi lr B_{SX}^2\tau}{4\mu_0}\cos(2\omega t - 2\lambda - \gamma_s) \end{aligned} \tag{13}$$

Analyzing Equation (13), it is shown that:

a. Where terms 1, 2, 3, 5 are major components of controllable suspension force; the latter three terms are nonlinear function of eccentricity τ (vibration eccentricity, static eccentricity or combination of them are defined as τ); terms 4, 6, 7 exciting vibration of stator and rotor are periodic function of 2ω.

b. Where terms 1, 2, 3, 4 are mutual reacted by torque current component and suspension current component. They are radial suspension force, generated by asymmetric air gap magnetic field. Among them, terms 1, 2, 3 exist only when $p_1 - p_2 \pm 1 = 0$. Term 4 is existed only when $p_1 + p_2 = 3$. Term 1 is suspension force, generated by the coactions of air gap magnetic field from torque current component and suspension current component in even air gap. The other three terms are generated by rotor eccentricity.

c. Where terms 5, 6, 7 are respectively generated by rotor eccentricity with torque current component and suspension current component. Among them, term 5 has nothing to do with number of pole pairs on current component. Term 6 exists only when $p_1 = 1$. Term 7 exists only when $p_2 = 1$.

In practical process of the single-winding bearingless induction motor, because the value of x and y are little, quadratic term and product term of them are neglected [14]. So the simplified model of radial suspension force can be expressed as:

$$\begin{aligned} f_x &= \frac{\pi l r B_{TX} B_{SX}}{2\mu_0} \cos(\mu - \lambda) + \frac{\pi l r \tau \left(B_{TX}^2 + B_{SX}^2\right)}{2\mu_0} \cos\gamma_s + \frac{\pi l r B_{TX}^2 \tau}{4\mu_0} \cos\left(2\omega t - 2\mu - \gamma_s\right) \\ &\quad + \frac{\pi l r B_{SX}^2 \tau}{4\mu_0} \cos\left(2\omega t - 2\lambda - \gamma_s\right) \end{aligned} \tag{14}$$

In the same way:

$$\begin{aligned} f_y &= \frac{\pi l r B_{TX} B_{SX}}{2\mu_0} \sin(\mu - \lambda) + \frac{\pi l r \tau \left(B_{TX}^2 + B_{SX}^2\right)}{2\mu_0} \sin\gamma_s + \frac{\pi l r B_{TX}^2 \tau}{4\mu_0} \sin\left(2\omega t - 2\mu - \gamma_s\right) \\ &\quad + \frac{\pi l r B_{SX}^2 \tau}{4\mu_0} \sin\left(2\omega t - 2\lambda - \gamma_s\right) \end{aligned} \tag{15}$$

According to the above mathematical model of radial suspension force, the following conclusions can be drawn:

a. In Equations (14) and (15), term 1 is a controllable component of radial suspension force, which is generated by the single winding. The air gap flux density of torque, air gap flux density of suspension and generation of sine and cosine from angle of them are proportional to the numerical magnitude.

b. In Equations (14) and (15), term 2 is eccentricity magnetic force which is generated by eccentric rotor. The center displacement is linearly proportional to the numerical magnitude. Terms 3 and 4 are also eccentricity magnetic force which is generated by eccentric rotor. The rotor eccentric components of x and y are nonlinearly proportional to the numerical magnitude, which are intercoupling. In the equations, terms 2, 3 and 4 are named as non-controllable components of radial suspension force, which are difficult to control artificially.

Below, the controllable radial suspension force based on non-eccentricity is considered.

$$\begin{cases} f_x = \dfrac{\pi l r}{2\mu_0} B_{TX} B_{SX} \cos(\lambda - \mu) \\ f_y = \dfrac{\pi l r}{2\mu_0} B_{TX} B_{SX} \sin(\lambda - \mu) \end{cases} \tag{16}$$

When the torque current component or suspension current component is injected alone in the rotor, $f_x = f_y = 0$, and the Maxwell force is 0. When the rated value is chosen as torque current component, changing the suspension current component, F_{math} can be figured out. f_x and f_y are sine function and cosine function. The amplitude of F_{math} can be defined as:

$$F_{\text{math}} = \frac{\pi l r}{2\mu_0} B_{TX} B_{SX} \tag{17}$$

4. THE FINITE ELEMENT ANALYSIS ON MATHEMATICAL MODEL OF RADIAL SUSPENSION FORCE BASED ON TWO FUNDAMENTAL WAVE METHOD

1) Motor Parameter

The number of stator slots is 36. The number of the conductors in every groove winding is 31. Inner diameter of the stator is 98 mm. External diameter of the stator is 155 mm. Inner diameter of the rotor is 36 mm. External diameter of the rotor is 97.8 mm. Length of the stator core is 155 mm. Slip ratio is 3%, and synchronous speed is 6000 r/min.

2) Distribution of Magnetic Field on Motor

Based on the principle of Finite Element, 2D magnetic fields are analyzed by Ansoft/Maxwell. When the torque current component is injected in the single winding, magnetic field is produced shown

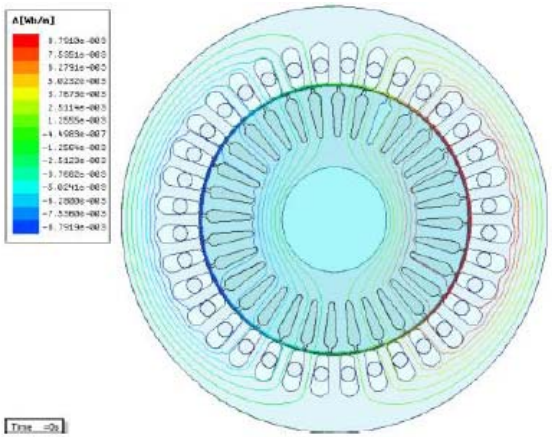

Figure 6. Magnetic field distribution of only existing torque component on stator winding.

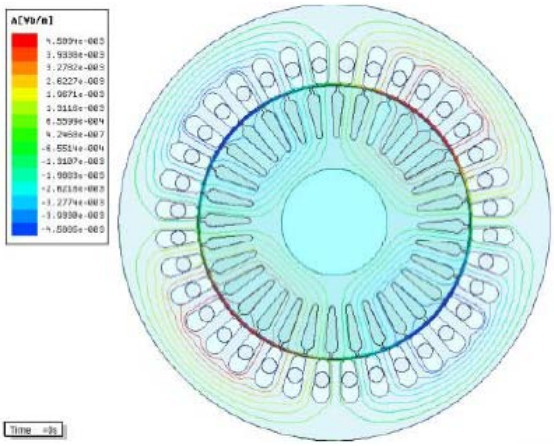

Figure 7. Magnetic field distribution of only existing suspension component on stator winding.

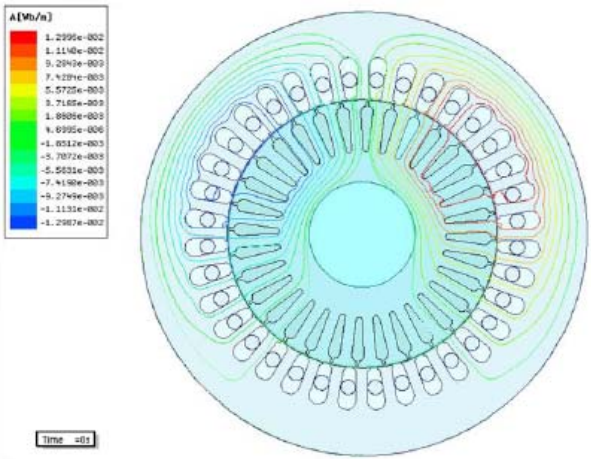

Figure 8. Magnetic field distribution of existing suspension component and torque component on stator winding.

in Fig. 6. When the suspension current component is injected in the single winding, magnetic field is produced shown in Fig. 7. When the torque current component and suspension current component are injected in the single winding at the same time, the composite magnetic field is produced along positive direction on y-axis shown in Fig. 8. As shown in Fig. 6 and Fig. 7, when the torque current component or suspension current component is injected alone in the single winding, magnetic field in the motor is distributed symmetrically, and the Maxwell resultant is 0. As shown in Fig. 8, when the torque current component and suspension current component are injected in the single winding at the same time, the magnetic field produced is superposed mutually, and distribution of magnetic field is uneven. Magnetic lines of force along positive direction on y-axis is dense, and magnetic induction is enhanced. Meanwhile, magnetic lines of force along negative direction on y-axis is sparse, and magnetic induction recedes. According to the producing principle of Maxwell force, suspension force along positive direction on y-axis is produced. Magnetic lines on force along x-axis is symmetrical, and resultant force along x-axis is 0. That is the same as the producing principle of Maxwell force preceding analysis, so the correctness of the producing principle of Maxwell force is verified.

3) The Finite Element Analysis on Radial Suspension Force

When torque current component is chosen, the rated value $I_T = 0.6\,\text{A}$, and when the suspension current component is chosen, the rated value $I_S = 1\,\text{A}$. When three-phase alternating current is injected in the single winding, the waveform curves of finite element (f_x and f_y) from the Maxwell are respectively

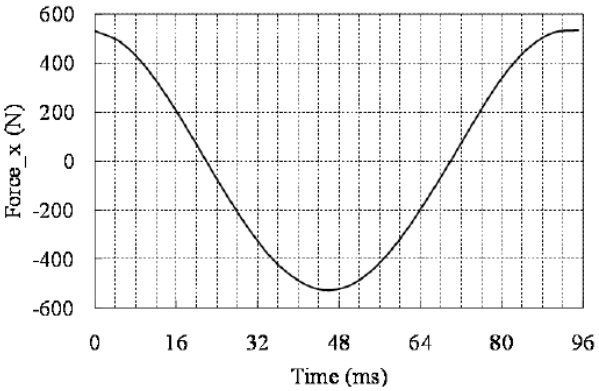

Figure 9. The finite element curve on f_x.

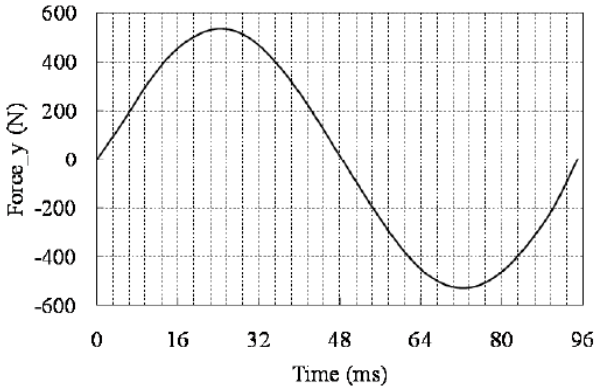

Figure 10. The finite element curve on f_y.

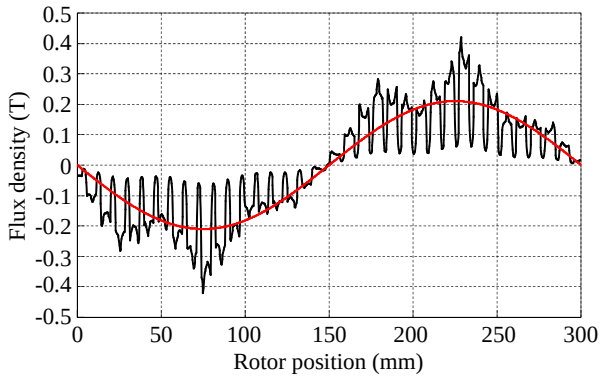

Figure 11. The waveform of air gap flux density when $I_T = 0.6\,\mathrm{A}$, $I_S = 0\,\mathrm{A}$.

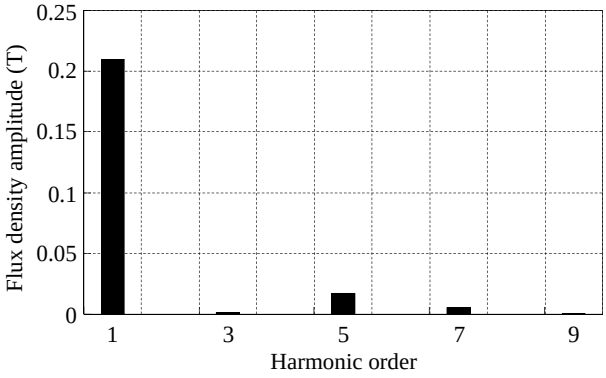

Figure 12. The harmonic column figure when $I_T = 0.6\,\mathrm{A}$, $I_S = 0\,\mathrm{A}$.

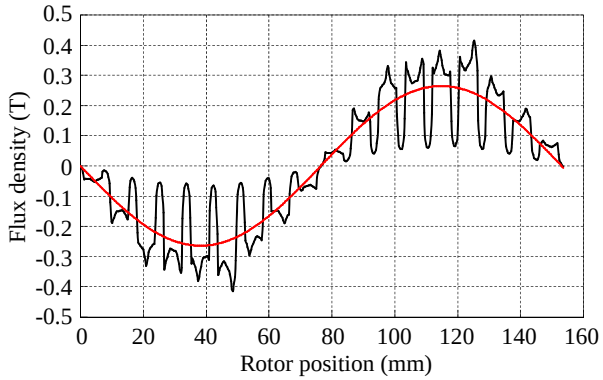

Figure 13. The waveform of air gap flux density when $I_T = 0\,\mathrm{A}$, $I_S = 1\,\mathrm{A}$.

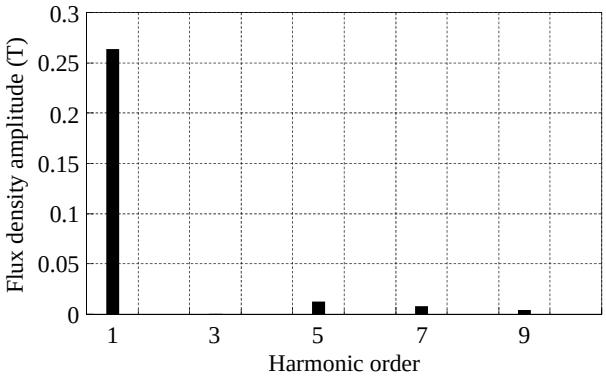

Figure 14. The harmonic column figure when $I_T = 0\,\mathrm{A}$, $I_S = 1\,\mathrm{A}$.

shown in Fig. 9 and Fig. 10.

According to the waveform curve of finite element (f_x and f_y), f_x is cosine curve and f_y sine curve. That is the same as the analysis conclusion from Equation (16), and the amplitude of radial suspension force is 530 N ($F_{\mathrm{finite}} = 530\,\mathrm{N}$).

4) Calculation of Mathematical Model on Radial Suspension Force Based on Two-Fundamental Wave Method

The amplitude of air gap magnetic density on torque current component and suspension current

component are named two-fundamental wave (B_{TX}, B_{SX}). If B_{TX} and B_{SX} are figured out, the amplitude of mathematical model on radial suspension force based on Equation (9) can be figured out.

When $I_T = 0.6\,\text{A}$ and $I_S = 0\,\text{A}$, the wave of air gap magnetic density is shown as Fig. 11, and FFT histogram used by Matlab is shown as Fig. 12.

According to Fig. 12, fundamental voltage amplitude of air gap magnetic density on motor is $0.213\,\text{T}$ ($B_{TX} = 0.213\,\text{T}$).

When $I_T = 0\,\text{A}$ and $I_S = 1\,\text{A}$, the wave of air gap magnetic density is shown as in Fig. 13, and FFT histogram used by Matlab is shown as in Fig. 14. According to the Fig. 14, fundamental voltage amplitude of air gap magnetic density on motor is $0.264\,\text{T}$ ($B_{SX} = 0.264\,\text{T}$). B_{TX} and B_{SX} are substituted in Equation (17), and F_{math} can be figured out ($F_{\text{math}} = 533\,\text{N}$).

5) The Comparative Analysis between Finite Element Value and Mathematics Calculation Value

F_{finite} and F_{math} above are almost equal and have minor errors. In other words, when $I_T = 0.6\,\text{A}$ and $I_S = 1\,\text{A}$, the finite element waveform curve is the same as that of the mathematical model. The general situation is analyzed below.

Table 1 is given when $I_T = 0.6\,\text{A}$ (I_T is taken as the rating value), $B_{TX} = 0.213\,\text{T}$, $I_S \leq 1\,\text{A}$, and motor's parameters are $l = 155\,\text{mm}$, $r = 97.8\,\text{mm}$. The amplitude of radial suspension force based on finite element analysis (F_{finite}) and amplitude of radial suspension force based on mathematical model (F_{math}) are changed as in Table 1.

The data in Table 1 are drawn into points. Those points are connected into lines such as in Fig. 15.

Table 1. The value of F_{math} and F_{fem} (I_T is taken as the rating value and I_S is taken as variable).

I_S/A	B_{SX}/T	F_{math}/N	F_{fem}/N
0	0	0	0
0.1	0.028	58	57
0.2	0.057	117	114
0.3	0.088	176	174
0.4	0.116	233	230
0.5	0.137	275	273
0.6	0.166	338	335
0.7	0.194	395	393
0.8	0.226	456	452
0.9	0.250	504	502
1	0.264	533	530

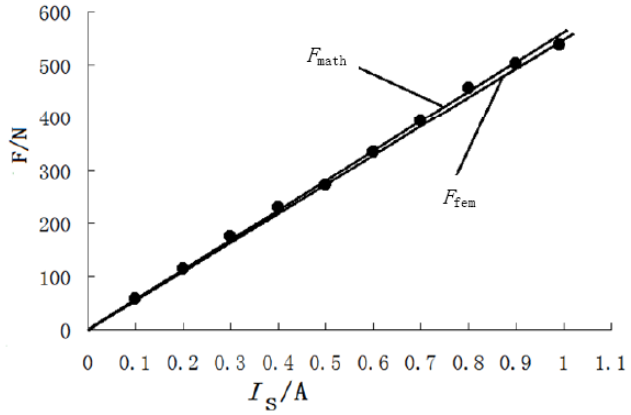

Figure 15. The comparison curve between the two methods.

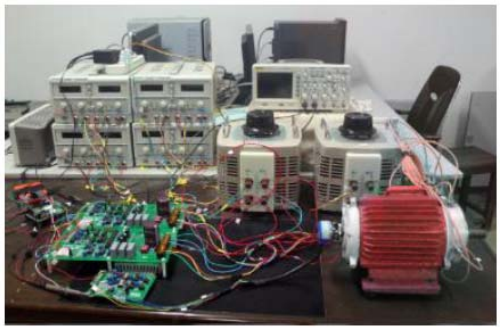

Figure 16. Digital control system.

In Fig. 15, comparing two lines, when $I_T = 0.6\,\mathrm{A}$ and $I_S \leq 1\,\mathrm{A}$, F_{finite} and F_{math} are almost increased straightly following increased I_S. The saturated relationship does not exist, and they are almost equal. Because of considered magnetic saturation, eddy current loss, stator magnetic potential harmonic and slot effect, the finite element value used by Ansoft is slightly smaller than mathematical calculated value. So the method of finite element is closer to the truth. Due to the comparison, the correctness of radial suspension force based on the two-fundamental wave method is verified. The foundation of optimization and control further is put forward for the single-winding bearingless induction motor.

5. THE SUSPENSION TEST AND CHARACTERISTICS ANALYSIS

According to the new structure of the single-winding bearingless induction motor which is put forward above, a experimental prototype and test platform about digital control system are made. Proceeding with suspension test, suspension characteristics are verified, and suspension force is analyzed. Parameters of the experimental prototype are used as follows: rated speed ($n = 6000\,\mathrm{r/min}$), rotational inertia ($J = 0.00769\,\mathrm{kg{\cdot}m^2}$), mass of rotor ($m = 2.85\,\mathrm{kg}$), outside diameter of rotor ($r = 97.8\,\mathrm{mm}$), core length ($l = 155\,\mathrm{mm}$). Material object on test platform is shown in Fig. 16. The dc power supply, experimental prototype, digital signal processor (TMS320F2812), radial displacement sensor, encoder, detection circuit and oscilloscope are included in the test platform.

A block diagram of the digital control system is shown in Fig. 17. As shown in Fig. 17, the system in this paper is compartmentalized into three parts: torque control part, suspension control part and current superposition control part.

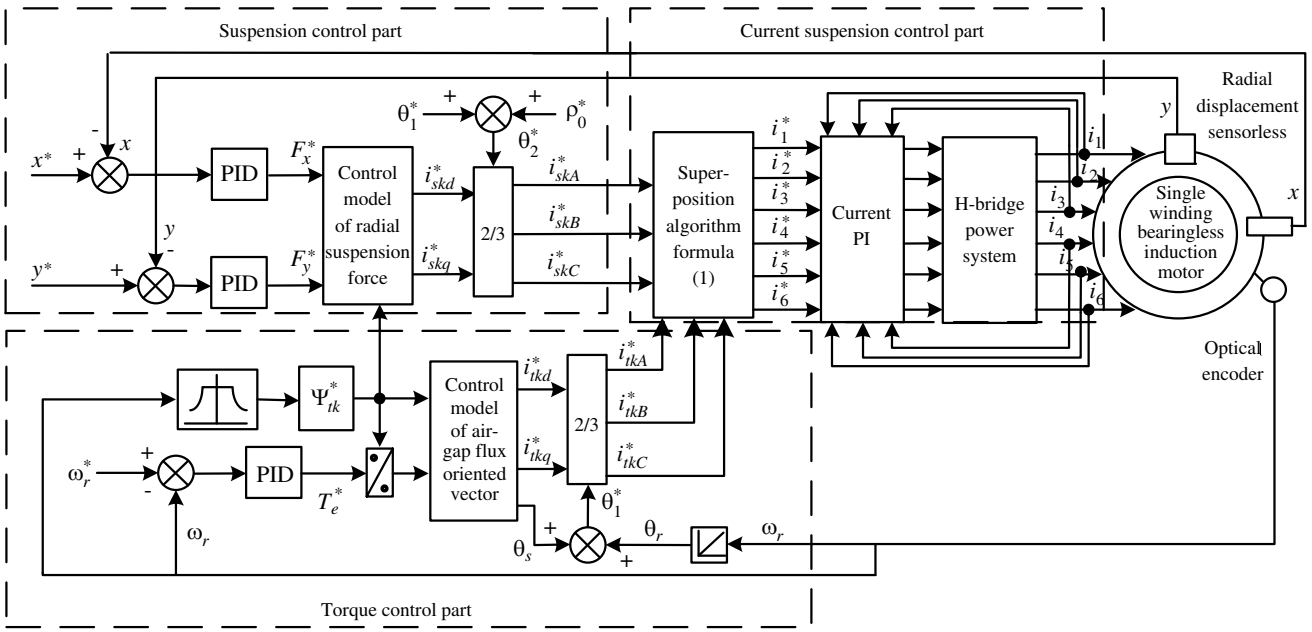

Figure 17. Block diagram of the digital control system.

In no-load suspension experiment, the speed of the single-winding bearingless induction motor is set as 3000 r/min. According to the test platform, suspension test precedes. The test results are shown following:

The oscillogram about speed response of rotor is shown in Fig. 18. According to the curve on speed response, the speed response of the rotor is better, and the given rotating speed is achieved at 3000 r/min in 1.2 s. The speed waveform is smooth, and the stabilization error is smaller.

After the rotor is in stable suspension working, the speed is achieved at 3000 r/min. When the rotor is in stable suspension working, the relationship oscillogram about radial migration with x direction and

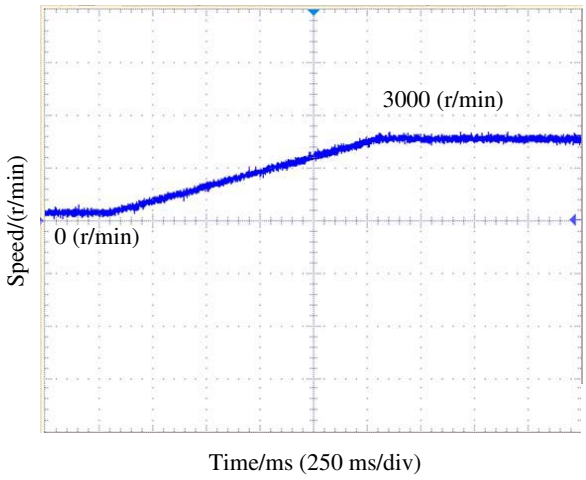

Figure 18. Speed response.

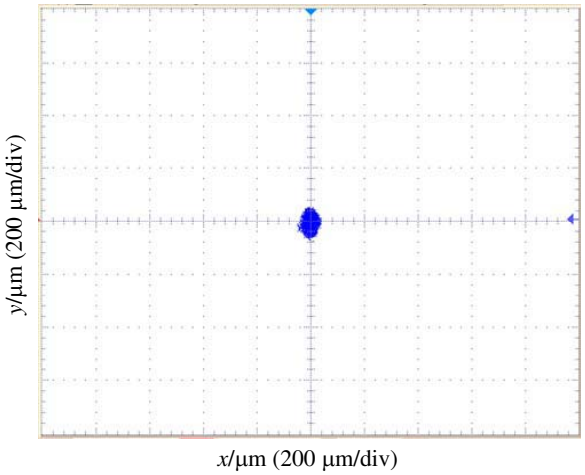

Figure 19. Displacement diagram.

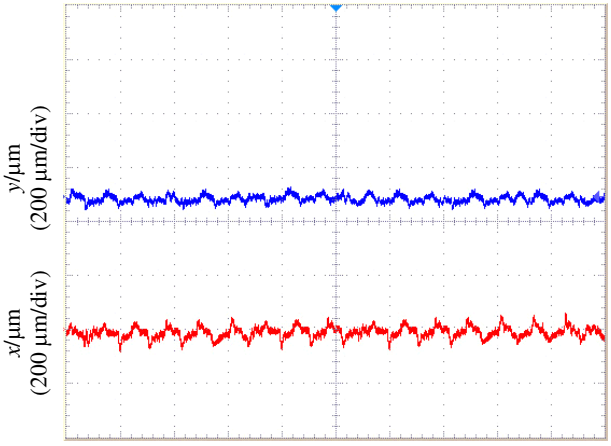

Figure 20. Radial displacement.

Table 2. Comparison of radial suspension force on x-axis.

I_s/A	Finite element method/N	Mathematical model Method/N	Measurement/N	Error/N
0.2	114	117	110	7
0.4	230	235	220	15
0.6	335	338	318	20
0.8	452	458	429	29

radial migration with y direction is shown as in Fig. 19. The migration about radial migration with x direction and y direction is shown in Fig. 20. According to Fig. 19 and Fig. 20, the range of amplitude is less than 80 μm, and the rotor has great suspension characteristics.

In load suspension experiment, the weight is hooked up to the shaft extension of suspension end. Torque current component is input in the stator winding. Regulating the radial suspension current component which produces the radial suspension force, eccentric rotor appears. Meanwhile, the quality of weight is controlled, which is used to keep the rotor in a balanced position. According to the quality of weight, the experimentally magnetic force can be measured. When $I_T = 0.6$ A (the rated current

Table 3. Comparison of radial suspension force on y-axis.

I_s/A	Finite element method/N	Mathematical model Method/N	Measurement/N	Error/N
0.2	113	117	107	10
0.4	231	233	219	14
0.6	333	338	316	22
0.8	453	456	430	26

value of the torque current component is 0.6 A) and $I_S \leq 1$ A, the calculation results on finite element method about controllable radial suspension force at x direction and at y direction, calculation results about mathematical model and the results about actual measurement are shown in Table 2 and Table 3.

According to Table 2 and Table 3, the calculation results about mathematical model established by two-fundamental wave method, the results from finite element method and the results from laboratory measurement are almost the same.

6. CONCLUSION

In a traditional bearingless induction motor, the insulation in windings is required strictly in which the complexity of motor design and proceeding is increased. A new structure of a single-winding bearingless induction motor is researched. Aiming at the question in which the exact mathematical model is difficult to calculate, the research method on radial suspension force based on two-fundamental wave method is put forward. Manufacturing the prototype and proceeding with the suspension test, results from experimental measurement, finite element method and mathematical model are compared. In suspension experiment, the prototype can be suspended stably. The prototype possesses excellent characteristics. The conclusion is as below:

1) Compared to the universal radial suspension models of bearingless motor, owing to the mathematical model of radial suspension force based on two-fundamental wave method, the foundation is provided for accurate calculation of mathematical model on radial suspension force in a single-winding bearingless induction motor. And the basis is provided for the control method of a single-winding bearingless induction motor.
2) Compared to the modeling approaches on radial suspension models of traditional dual-windings bearingless induction motor, owing to the research method solution based on two-fundamental wave method, considered various comprehensive factors of single-winding bearingless induction motor in simulation, establishing process is simple, easy with high precision. And the measurement of radial suspension force is more convenient in experiment.

ACKNOWLEDGMENT

This work was supported by the National Natural Science Foundation of China under Projects 51475214, 51305170, the China Postdoctoral Science Foundation funded project under Projects 2015T80508 and 2014T70482, the Natural Science Foundation of Jiangsu Province of China under Projects BK20130515, BK20141301 and BK20150524, the Professional Research Foundation for Advanced Talents of Jiangsu University under Projects BK20150524 and 14JDG076, the Six Categories Talent Peak of Jiangsu Province under Project ZBZZ-017, and the Priority Academic Program Development of Jiangsu Higher Education Institutions.

REFERENCES

1. Xu, B., H. Q. Zhu, W. Ji, et al., "Rotating high frequency signal injection method based on FIR optimization filter and its application," *Chinese Journal of Scientific Instrument*, Vol. 33, No. 3, 589–595, 2012.

2. Sun, X. D., L. Cheng, Z. B. Yang, et al., "Speed-sensorless vector control of a bearingless induction motor with artificial neural network inverse speed observer," *IEEE/ASME Transactions on Mechatronics*, Vol. 18, No. 4, 1357–1366, 2013.
3. Li, B. N., J. Huang, M. Kang, et al., "Analysis and comparison of inductance and suspension force for 2-4 type and 4-2 type multiphase permanent magnet bearingless motors," *Proceedings of the CSEE*, Vol. 33, No. 33, 106–114, 2013.
4. Bu, W. S., C. L. Zu, S. J. Wang, et al., "MRAS speed identification of bearingless induction motor based on rotor flux orientation," *Control Engineering of China*, 2014.
5. Silber, S., W. Amrhein, et al., "Design aspects of bearingless slice motors," *IEEE/ASME Transactions on Mechatronics*, Vol. 10, No. 6, 611–617, 2005.
6. Zhu, J., Z. Q. Deng, X. L. Wang, et al., "Principle and implementation of the single winding bearingless permanent magnetic slice motor," *Proceedings of the CSEE*, Vol. 28, No. 33, 68–74, 2008.
7. Asama, J., Y. Hamasaki, T. Oiwa, et al., "Proposal and analysis of a novel single-drive bearingless motor," *IEEE Transactions on Industrial Electronics*, Vol. 60, No. 1, 129–138, 2013.
8. Sun, D. S., B. M. Ge, W. L. Wu, et al., "Modeling and control of induction machines with pole-phase modulation," *Proceedings of the CSEE*, Vol. 32, No. 18, 80–87, 2012.
9. Zhu, H. Y., J. T. Hu, L. Gao, et al., "Fault diagnosis of incipient broken rotor bars for squirrel-cage induction motor under continuous variable load condition," *Chinese Journal of Scientific Instrument*, Vol. 35, No. 7, 1646–1653, 2014.
10. Huang, J., B. Li, H. Jiang, et al., "Analysis and control of multiphase permanent-magnet bearingless motor with a single set of half-coiled winding," *IEEE Transactions on Industrial Electronics*, Vol. 61, No. 7, 3137–3145, 2014.
11. Bu, W. S., S. M. Wan, S. H. Huang, et al., "General analytical model about controllable magnetic suspension force of bearingless motor," *Proceedings of the CSEE*, Vol. 29, No. 30, 84–89, 2009.
12. Zuo, W. Q., Y. B. Lv, X. D. Fu, et al., "Accurate mathematical modeling of radial suspension force on bearingless permanent magnet slice motors," *Proceedings of the CSEE*, Vol. 32, No. 3, 103–110, 2012.
13. Kong, X. and L. Wang, "An adaptive parameter decoupling control method for bearingless synchronous reluctance motor," *2014 11th World Congress on IEEE Intelligent Control and Automation (WCICA)*, 4572–4576, 2014.
14. Zhang, H., H. Zhu, Z. Zhang, et al., "Design and simulation of control system for bearingless synchronous reluctance motor," *Proceedings of the Eighth International Conference on IEEE Electrical Machines and Systems, 2005, ICEMS 2005*, 554–558, 2005.